Velocity Gradients of the African Large Low Velocity Province Boundary Inferred from Backazimuth-Slowness Observations of Multipathing

Jamie Ward[1], **Andy Nowacki**[1], **Sebastian Rost**[1]

[1]School of Earth and Environment, University of Leeds

Key Points:

- Multipathing is observed using backazimuth and horizontal slowness measurements of SKS and SKKS data recorded in southern Africa.
- Lateral velocity gradients of up to 0.7% δV_s per 100 km (0.00050 km s^{-1} km^{-1}) are required to produce the observed multipathing.
- Lateral velocity gradients capable of producing multipathing cannot distinguish between thermal and thermochemical LLVP models.

Corresponding author: Jamie Ward, eejwa@leeds.ac.uk

Abstract

Large Low Velocity Provinces (LLVPs) are hypothesised to be purely thermal features or possess some chemical heterogeneity, but exactly which remains ambiguous. Regional seismology studies typically use travel time residuals and multipathing identification in the waveforms to infer properties of LLVPs. These studies have not fully analysed all available information such as measuring the direction and inclination of the arrivals. These measurements would provide more constraints of LLVP properties such as the boundary velocity gradient and help determine their nature. Here, we use array seismology to measure backazimuth (direction) and horizontal slowness (inclination) of arriving waves to identify structures causing multipathing and wavefield perturbation. Following this, we use full-wavefield forward modelling to estimate the gradients required to produce the observed multipathing. We use SKS and SKKS data from 83 events sampling the African LLVP, which has been extensively studied providing a good comparison to our observations. We find evidence for structures at heights of up to 600 km above the core-mantle boundary causing multipathing and wavefield perturbation. Forward modelling shows gradients of up to 0.7 % δV_s per 100 km (0.0005 km s^{-1} km^{-1}) are required to produce multipathing with similar backazimuth and horizontal slowness to our observations. This is an order of magnitude lower than the previous strongest estimates of -3 % δV_s per 50 km (0.0044 kms^{-1} km^{-1}). As this is lower than found for both thermal and thermochemical structures, gradients capable of producing multipathing is not necessarily evidence for a thermochemical nature.

Plain Language Summary

Of the structures observed within the Earth, 'Large Low-Velocity Provinces' (LLVPs) have remained enigmatic in terms of their composition and origin. LLVPs have been hypothesised to affect the Earth from surface uplift to influencing the magnetic field. Determining what LLVPs are remains a major question for those studying Earth structure.

Previous seismology studies analysing LLVPs used the time taken for the wave to travel from the earthquake to the recording station and what the seismic signals look like when they arrive. However, properties such as the direction and speed at which the waves arrive are not analysed in detail. The speed and direction of the waves can inform us about how LLVPs have perturbed the waves by phenomena such as refraction.

This study measures the direction and speed of the arriving waves that have sampled the LLVP beneath Africa. Analysing this information has lead to several structures to be identified. From modelling the full wavefield with different LLVP models, we estimate the distance over which the transition from the mantle to the LLVP happens. To replicate our observed changes in direction and speed of the waves, the transition could be 10% larger than previous estimates.

1 Introduction

Large Low Velocity Provinces (LLVPs) are roughly antipodal, low-velocity features of the lower mantle located beneath Africa and the Pacific and are surrounded by high velocity material hypothesised to be slab remnants (Bijwaard et al., 1998; Grand et al., 1997; Grand, 2002), shown in Figure 1. Since first observed, LLVPs have remained enigmatic features of the lower mantle with their origin, composition and therefore their influence remaining uncertain.

The location of the LLVPs relative to other structures and phenomena such as surface uplift (Hager et al., 1985; Lithgow-Bertelloni & Silver, 1998; Bull et al., 2010), possible subducted slab remnants (Hager, 1984), mantle plumes (Thorne et al., 2004; Davies, Goes, & Sambridge, 2015), large igneous provinces (Torsvik et al., 2010), Ultra Low Velocity Zones (McNamara et al., 2010) and outer core stratification (Mound et al., 2019) suggests LLVPs are influential on whole Earth dynamics. Despite being very significant for our understanding of global dynamics, many properties of the LLVPs are still unknown and there are several hypotheses of their origin. These hypotheses can be approximately split into those where LLVPs are purely thermal features and those in which they are chemically distinct relative to the surrounding mantle (Garnero et al., 2016). For a purely thermal feature, a common hypothesis is that LLVPs are a cluster of plumes (Schubert et al., 2004) which appear as one large slow feature because of the inherent resolution limitations from seismic tomography (Bull et al., 2009; Ritsema et al., 2007; Davies et al., 2012; Davies, Goes, & Lau, 2015). The thermochemical origin hypothesis requires a source of material chemically unique to the current lower mantle either from the primordial Earth or material that has accumulated over geological time. Material from the primordial Earth is hypothesised to start as a basal layer of material that is swept into piles forming the LLVPs. Mechanisms for the origin of this base layer include a basal magma ocean (Labrosse et al., 2007), accumulation of dense melts (Lee et al., 2010) or an ancient, iron enriched crust which was then subducted and is stable at CMB conditions (Tolstikhin & Hofmann, 2005). This basal layer could then have been swept into piles observed as LLVPs which has been shown numerically (Tackley, 1998) and experimentally (Davaille, 1999). Alternatively, they could have accumulated over geological time as subducted lithosphere in the lower mantle (Hirose et al., 1999, 2005; Christensen & Hofmann, 1994) which is swept into piles, forming the LLVPs (Mulyukova et al., 2015; Tackley, 2011). However, there is some question of the feasibility of producing negative velocity perturbations (Deschamps et al., 2012) and for the slab material to accumulate at the same rate as it is stirred into the mantle (Li & McNamara, 2013).

Depending on the origin of the LLVPs, our understanding of how the Earth evolved from its primordial state changes. If LLVPs are a short-lived cluster of mantle plumes, they do not need to exist in early Earth history. If they are long-lived piles of primordial Earth remnants, their formation and survival would need to be accounted for. Constraining the origin of LLVPs therefore has implications for our understanding of the Earth's history as well as whole Earth dynamics.

To reduce the number of hypotheses, there has been a focus on determining whether LLVPs are purely thermal or thermochemical features. Their relative density could provide constraints but conflicting observations have suggested both higher and lower relative density (Koelemeijer et al., 2017; Ishii & Tromp, 1999; Lau et al., 2017). Anticorrelation of S-wave velocity and bulk sound speed (Masters et al., 2000; Su & Dziewonski, 1997) is commonly used as evidence for compositional heterogeneity for LLVPs, but this has also been interpreted as the presence of post-perovskite (Davies et al., 2012; Koelemeijer et al., 2015). The presence of strong lateral velocity gradients has been attributed to a thermochemical origin (Ni et al., 2002; To et al., 2005), but these gradients can also be replicated with purely thermal structures (Davies et al., 2012; Schuberth et al., 2009).

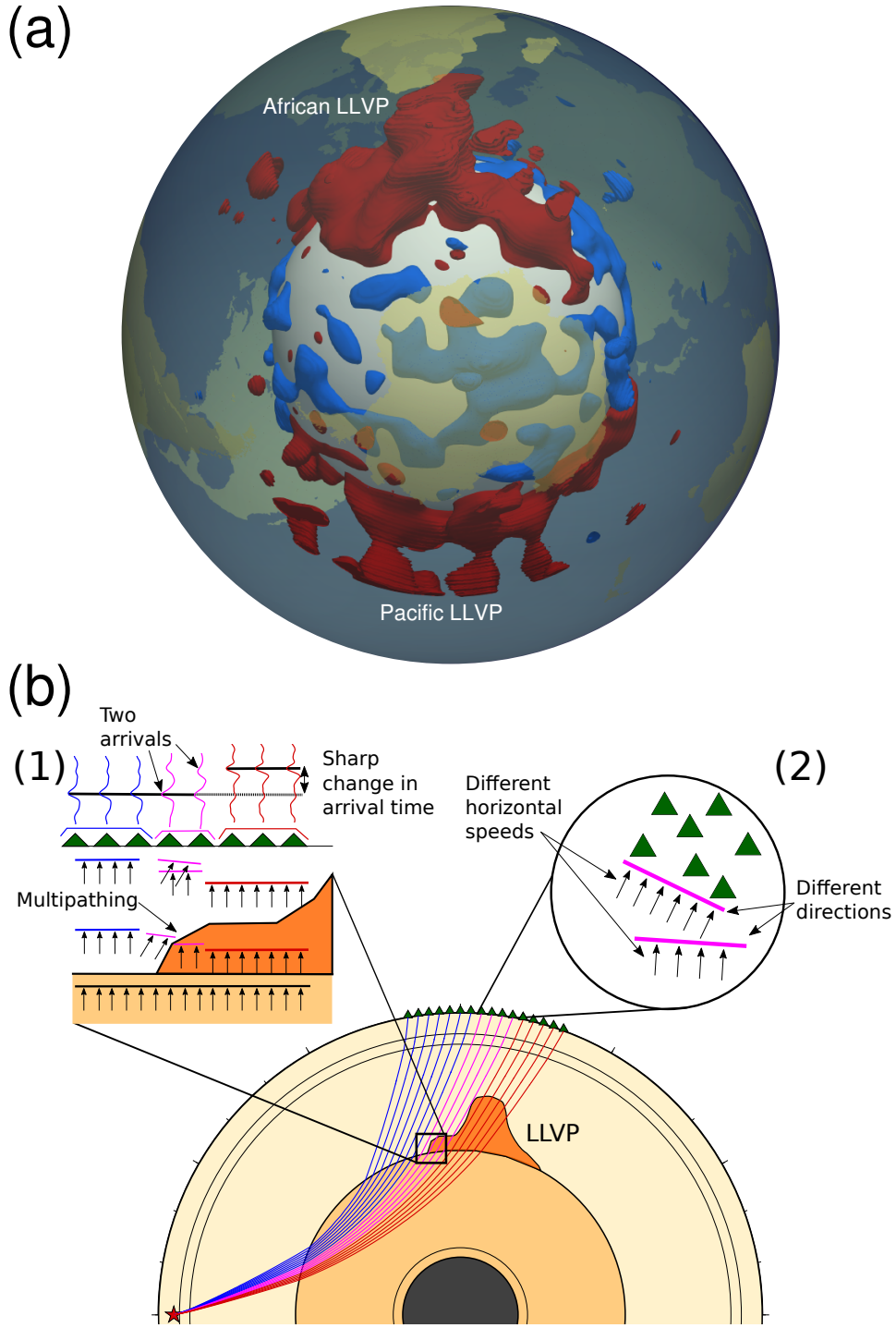

Figure 1. **(a)** 3D map of tomography model SEMUCB-WM1 (French & Romanowicz, 2014) with an isosurface of -1% δ V_s shown in red and an isosurface of $+1\%$ δV_s in blue. The isosurface is plotted below 80% of the Earth's radius (5097 km, 2205 km above the CMB). **(b)** Multipathing at LLVP boundaries. As the wavefront moves over a strong lateral velocity gradient, different parts travel at different speeds and arrive at the stations at different times as two distinct arrivals **(1)**. The gradients can cause the wave to diffract and the structure can cause the wave to refract as it passes through it. As a result, multipathed arrivals can arrive from different directions and inclinations **(2)**.

Most of these studies use observations or constraints from seismological studies. Seismic tomography provides global, broad observations of LLVP location, morphology and relative velocity (e.g. French & Romanowicz, 2014; Ritsema et al., 2011; Simmons et al., 2010; Grand, 2002; Grand et al., 1997; Koelemeijer et al., 2015). The agreement of the long wavelength structure of LLVPs in tomography models shows they are a result of lower-mantle structure and not the different datasets or methodologies used (Lekic et al., 2012). In addition to these global observations, regional seismology studies combine travel time residuals, multipathing observations in the waveform and forward modelling to recover the location, gradient and inclination of LLVP boundaries (e.g. Ni et al., 2002; Ritsema et al., 1998; Sun & Miller, 2013; He & Wen, 2009; He et al., 2006; He & Wen, 2012; To et al., 2005; Frost & Rost, 2014; Roy et al., 2019). Multipathing occurs when a wavefront is incident on a strong lateral velocity gradient that causes the wavefront to move at different speeds and arrive at a recording station with different travel times as two arrivals. In addition to this, the boundary structure causes the wave to diffract and the structure causes the waves to refract as they pass through it, so the multipathed arrivals arrive from different directions and inclinations as well as arrival times. Figure 1 illustrates the multipathing phenomena at LLVP boundaries and how they can be observed at the surface.

LLVP boundary studies using travel time residuals and waveforms are common and, from their observations, have estimated the gradients at the boundaries of LLVPs to range from 3 % δV_s per 50 km (0.0044 km s^{-1} km^{-1}) (Ni et al., 2002) to 2 % δV_s per 300 km (0.00048 km s^{-1} km^{-1}) (Ritsema et al., 1998) (See Table 1 for published estimates of African LLVP S-wave velocity gradients). Combining travel time residuals, multipathing identification and forward modelling to observe and infer the properties of structures is well established and has been applied to a variety of structures (Silver & Chan, 1986; Sun et al., 2019, 2010, 2017) and algorithms developed to identify multipathing automatically in the waveforms (Sun et al., 2009; Zhao et al., 2015). Although regional seismology studies only use the waveform to infer the effects of deep Earth structure on the wavefield, they do not analyse all information available such as the direction and inclination of the arrival.

Study	Gradient (δV_s)	Gradient (kms^{-1} km^{-1})
Ni et al. (2002)	−3% per 50 km	0.0044
Ni and Helmberger (2003c)	−3% per 100–150 km	0.0022 – 0.0015
Ni and Helmberger (2003a)	−3% per 50 km	0.0044
Sun and Miller (2013)	−3.5% per 200 km	0.0013
Ritsema et al. (1998)	−2% per 300 km	0.00048
This study	−0.7% per 100 km	0.00050

Table 1. Table of lateral gradients of the African LLVP's boundaries in δV_s and kms^{-1}km^{-1}. The gradients for kms^{-1}km^{-1} were calculated using the V_s value for PREM (Dziewonski & Anderson, 1981) at the CMB

Current observations have not been sufficient to constrain LLVP properties and therefore their composition, origin and influence remain ambiguous. Both purely thermal and thermochemical structures can replicate properties such as the strong gradients, veloc-

ity reduction, morphology and anticorrelation between S-wave velocity and bulk sound speed (Davies et al., 2012; Schuberth et al., 2009; Tackley, 1998; McNamara & Zhong, 2004, 2005; McNamara et al., 2010). Because current seismic observations are not enough to constrain LLVP properties, new observations need to be made.

This study uses array seismology to measure the backazimuth (direction) and horizontal slowness (a proxy for inclination) to identify multipathing and regions of diffraction and refraction in the lower mantle beneath Africa, where several studies have identified multipathing and sharp travel time residuals (e.g. Ni et al., 2002; Sun et al., 2009; Wen et al., 2001). Different frequency bands are used to infer differences in the African LLVP boundary structure such as gradient, depth and inclination. Using these observations, we estimate the gradients required to produce multipathing with similar backazimuth and horizontal slowness deviations as our observations and compare our estimates to those from previous studies.

148 ## 2 Methodology

149 ### 2.1 Slowness vector grid search and beamforming

150 To measure the backazimuth and horizontal slowness, we search over a range of slow-
151 ness vectors each with its own backazimuth and horizontal slowness and use beamform-
152 ing (Rost & Thomas, 2002) to measure the power of the coherent signal. If there are mul-
153 tiple arrivals, we detect multiple arrivals with different backazimuth and horizontal slow-
154 ness. The results are referred to as $\theta-p$ plots as they describe how the power of coher-
155 ent signal varies with backazimuth (θ) and horizontal slowness (p). Figure 2 shows ex-
156 amples of clear, possible and null multipathing observations. The analysis is conducted
157 within a time window selected from visual inspection of record section, typically on the
158 order of tens of seconds. Information such as the time windows, stations, measurements,
multipathing identification are in the supplementary material.

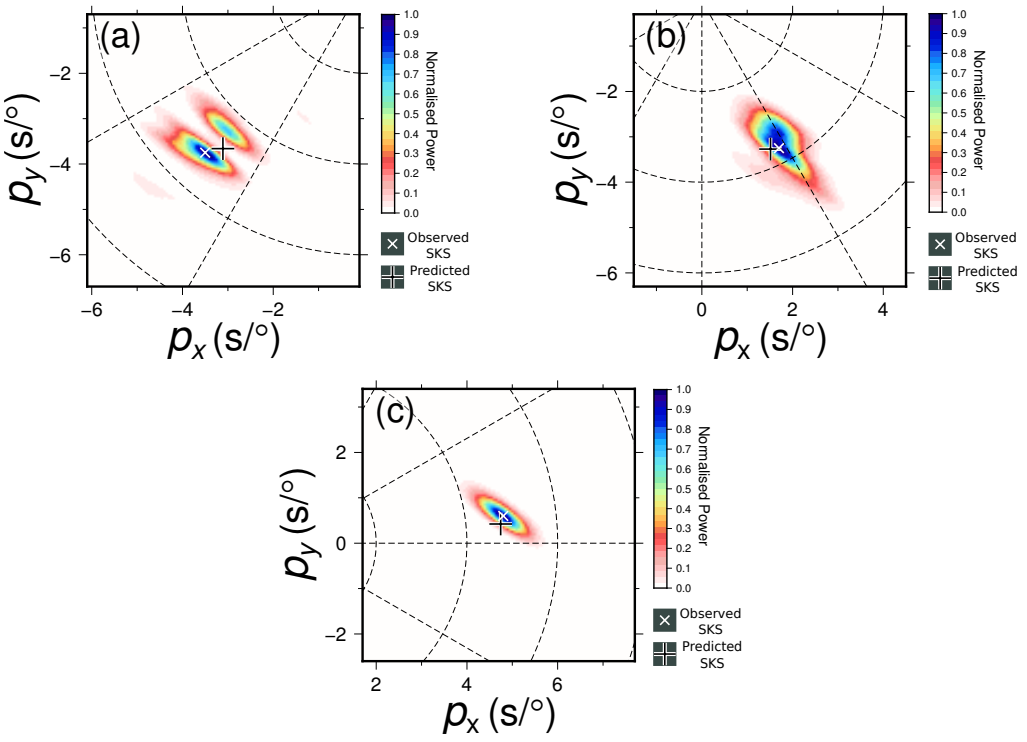

Figure 2. θ–p plots giving examples of arrivals classified as **(a)** clear multipathing using data from an event on 29 May, 1997, **(b)** potential multipathing using data from an event on 25 May, 1997 and **(c)** no multipathing using data from an event on 06 October, 1997. Details of event location and date are provided in the supplementary material. All of these were filtered between 0.10 and 0.40 Hz and the power linearly normalised.

159

160 Most array techniques assume energy propagates as a plane wavefront (Rost & Thomas,
161 2002). If the array aperture is small, this assumption holds and the effect of a curved
162 wavefront is negligible. We use data from the Kaapvaal array (James et al., 2001), which
163 has a large aperture (spread over approximately 20° in northwest-southeast orientation)
164 so the plane wave assumption breaks down and can contribute to some deviation from
165 the predicted backazimuth and horizontal slowness.

We alter the travel time calculation of beamforming to account for a circular wavefront given a backazimuth and horizontal slowness (Figure 3). To calculate the travel times of a circular wavefront moving over a spherical Earth from event to station locations, the radial distances are calculated using the Haversine formula. This distance is then multiplied by an angular slowness value in $s/°$. From these estimates, the traces are shifted, stacked and the power of the coherent signal estimated. To search over backazimuth, the event is relocated keeping the epicentral distance between the assumed event location and the mean station location constant. From this new location, the radial distance to each station is calculated relative to the mean distance and the travel times calculated (see supplementary information).

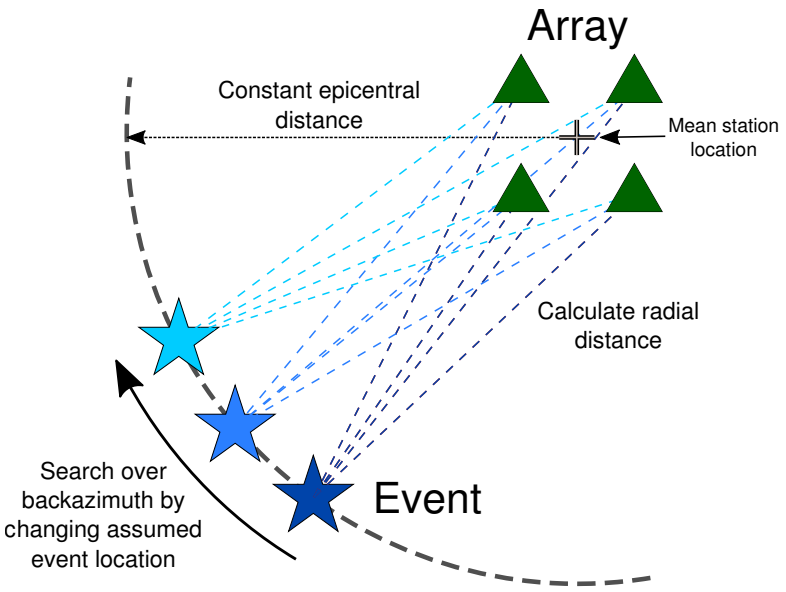

Figure 3. Illustration of the correction for a circular wavefront over a spherical Earth and how we search over backazimuth. The event location is changed depending on what backazimuth is tested with the epicentral distance kept the same. For each location, the radial distance to each station is calculated and the product of this with the angular slowness gives a travel time estimation.

We test our correction on synthetic data arriving from a known backazimuth and horizontal slowness (see supplementary information for further details and figures). We find our correction reduces the backazimuth deviation from 2.37° to 0.40° and the horizontal slowness deviation from 0.20 $s/°$ to 0.03 $s/°$.

2.2 Multipathing identification and slowness vector measurements

Multipathed arrivals are identified as power maxima separated in backazimuth and horizontal slowness and with a power value above the background noise and at least 10% of the maximum power value (Figure 2). The orientation is recorded for each observation with clear multipathing. We calculate the orientation of the locus between the multipathed arrivals relative to the vertical when multipathing is identified. This is calculated from the locations of the multipathed arrivals in the $\theta - p$ observation and calculating the angle of the vector connecting the two points relative to the vertical. This angle is then rotated by 90° as the locus is orthogonal to the vector connecting the two points.

Our data set includes SKKS phases (Section 2.4) at distances where other phases such as S3KS could arrive at similar times and horizontal slownesses, which make it challenging to identify multipathing. For SKKS observations where multipathing could be present, we analyse synthetics generated using SYNGINE and the 1-D model prem_i_2s (Hutko et al., 2017; Krischer et al., 2017) as an estimate of the relative power of SKKS and S3KS. If there is any power for an S3KS arrival in the synthetic $\theta-p$ plots and there are multiple arrivals in the recorded data, the observation is labeled as "possible" multipathing. See supplementary information for more details.

In addition to identifying multipathing, several measurements can be made from each observation. The backazimuth residual ($\Delta\Theta$) between the observed ($\Theta_{observed}$) and the backazimuth predicted by the great circle path between the event and mean station location ($\Theta_{predicted}$) is given by $\Delta\Theta = \Theta_{observed} - \Theta_{predicted}$. The horizontal slowness residual (Δp) between the observed ($p_{observed}$) and the PREM (Dziewonski & Anderson, 1981) predicted horizontal slowness ($p_{predicted}$) is given by $\Delta p = p_{observed} - p_{predicted}$. The vector from the predicted location to the observation location in the $\theta-p$ plot is recorded as a measure of the direction and strength of the perturbation the wave has experienced. Figure 4 illustrates the meaning of this vector residual, locus between the arrivals and visualises backazimuth and horizontal slowness deviations.

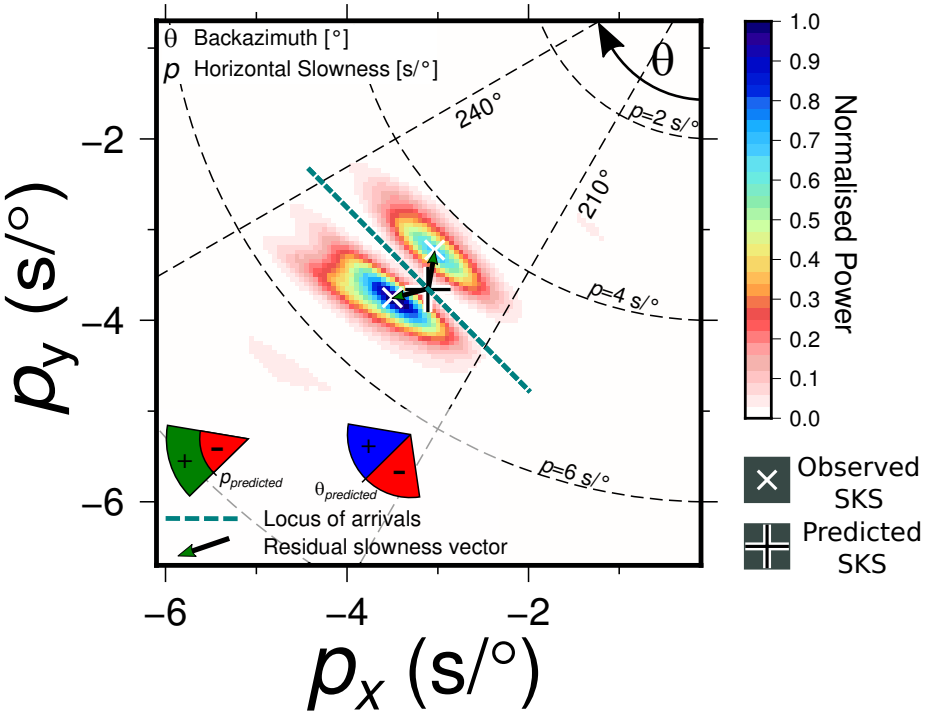

Figure 4. Annotations of the θ–p observation with data from an event on the 29 May, 1997 showing clear multipathing. The locus between the multipathed arrivals marked in blue gives an approximation of the boundary orientation. The residual slowness vector from the predicted backazimuth and horizontal slowness gives information of how the wavefield has been perturbed. Illustrations of positive and negative residuals for backazimuth and horizontal slowness are shown.

2.3 Frequency Analysis

To analyse the frequency dependence of multipathing and its wavefield effects, the data are filtered in five frequency bands and analysed separately (frequency bands: 0.07-0.28 Hz, 0.10-0.40 Hz, 0.13-0.52 Hz, 0.15-0.60 Hz, 0.18-0.72 Hz, 0.20-0.80 Hz) each with a width of two octaves. The frequencies will affect the size of the Fresnel zone, which gives an approximation of the area contributing to the observation. For both the main and multipathed arrival to have enough power to be observed, there needs to be a significant enough velocity change over the Fresnel zone. The frequency variation of multipathing could be indicative of differences in sharpness, depth or inclination between boundaries. Fresnel zones for each frequency band were calculated at the CMB using velocity value from PREM (Dziewonski & Anderson, 1981) and shown in the supplementary information.

2.4 Data and preprocessing

SKS and SKKS data (Figure 5) from events located 70° to 140° away from the centre of the array and with magnitudes between 5.5 and 7.5 recorded at the Kaapvaal array are used to analyse Africa LLVP boundary structure (Figure 5). We deconvolve the instrument response, remove the mean amplitude, taper and apply a bandpass filter between 0.05 and 1.0 Hz (period of $1-20$ s) for visual inspection. The horizontal components are rotated to radial and tangential components for clear SKS and SKKS identification. Following this, the signal-noise ratio (SNR) is estimated in a 70s time window around the predicted arrival time and used to roughly sort the data into traces that should be kept (SNR > 3), removed (SNR < 2.5) and could be used ($2.5 <$ SNR < 3). Events with more than 10 traces sorted into "keep" or more than half between the "keep" and the potentially usable bins were sorted by hand after visual inspection of the record section aligned on the PREM (Dziewonski & Anderson, 1981) predicted SKS arrival. If there is a clear SKKS arrival, SKKS is also analysed. 83 events remain (see supplementary material for event details).

The frequency bands we use are limited by the station spacing of the array. If the inter-station spacing is too large, spatial aliasing could occur in the $\theta - p$ plot and be misidentified as multipathing. The Nyquist criterion for the station spacing of each frequency band is used to limit the frequencies used. The lower frequencies will likely have higher amplitudes and influence the stacking significantly more than the higher frequencies, so we only limit the lower frequency cut offs for the frequency analysis using this criterion. The lower frequency cut-off is limited to 0.20 Hz.

2.5 Noise reduction techniques

Multipathed arrivals could arrive with a lower SNR and stack to a similar power as incoherent signal at other backazimuths and horizontal slownesses. To aid multipathing identification, several techniques to improve the SNR of coherent arrivals are implemented. We use phase weighted stacking (Schimmel & Paulssen, 1997), F-statistic (Blandford, 1974) and deconvolve the array response function (ARF) using the Richardson-Lucy deconvolution method (Richardson, 1972; Lucy, 1974) as done in previous studies (Picozzi et al., 2010; Maupin, 2011). These are detailed further in the supplementary information with examples of their effectiveness. We use the outputs of all these methods to identify multipathing in the data with criteria for clear, potential and no multipathing explained in Section 2.2. Measurements of horizontal slowness and backazimuth deviations are taken using the phase-weighted (Schimmel & Paulssen, 1997) stack points as they most consistently have lower noise than the other methods.

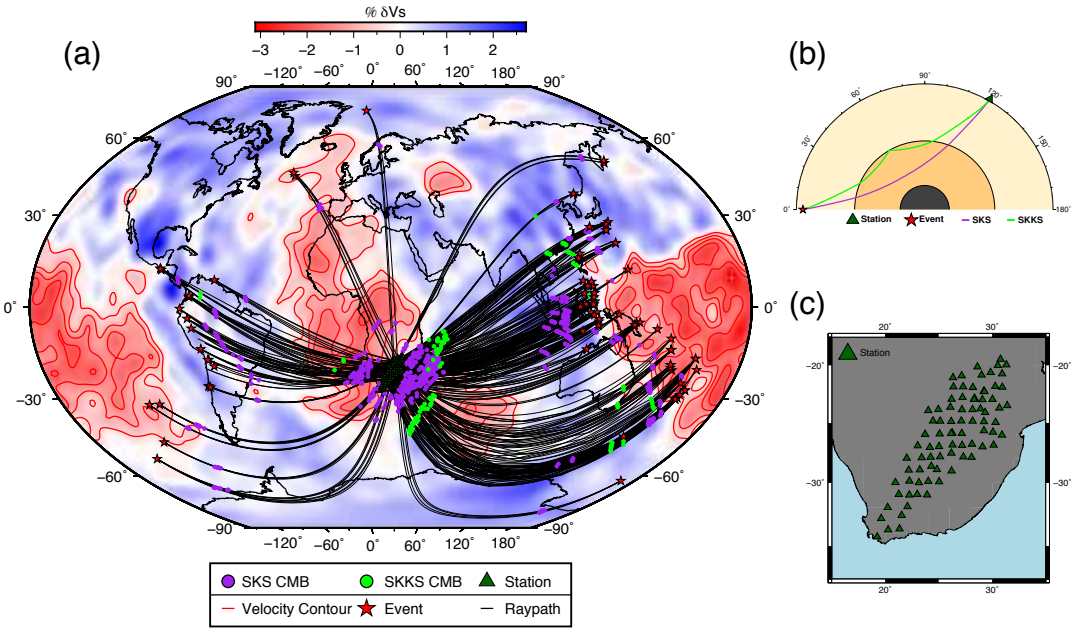

Figure 5. **(a)** The CMB pierce point locations for SKS and SKKS from events used in the analysis (Section 2.1) for whole array and sub array observations (Section 2.6). The earthquakes, stations and ray paths are also plotted to show what other structures could have been sampled. The paths provide good coverage of the African LLVP, its boundaries and the surrounding mantle. The pierce points are shown on tomography model S40RTS (Ritsema et al., 2011) with shear wave velocity contours of −0.5%, −1.0%, −1.5% and −2.0% δV_s marked to highlight potential boundaries and structure. **(b)** Paths of SKS (purple) and SKKS (green) though the Earth. **(c)** Station coverage of the Kaapvaal array, chosen for its excellent station density and coverage.

2.6 Sub arrays

To better constrain the location of multipathing and its wavefield effects, the available stations in the Kaapvaal array are grouped into sub arrays. Data from all available stations are also analysed. We group the traces using their waveform properties, backazimuths and epicentral distances. We accept that we are adding our own bias to the observations by grouping the sub arrays this way. Whole array observations are used to identify multipathing but, because the large area of the combined Fresnel zones of the Kaapvaal array, not used to analyse backazimuth and horizontal slowness deviations. 317 different sub array geometries were used; stations for each sub array are given in the supplementary material.

2.7 Method strengths and limitations

Other studies have developed a method to automatically detect multipathing in the waveform (Sun et al., 2009). In comparison to this method, there are several limitations and advantages. The multipathed arrivals need to be present in enough traces to stack coherently and produce clear arrivals on the $\theta - p$ plot. Arrivals of similar slowness may not be resolved as separate arrivals. On the other hand, noisier traces can be used because the stacking methods improve the SNR. The observations themselves also allow measurements of backazimuth and horizontal slowness deviations, which can be used to analyse structures affecting the wavefield.

3 Multipathing

This section describes our multipathing observations and discusses the frequency dependence (Section 3.1) and spatial variation (Section 3.2) with interpretations of possible boundary locations. Clear multipathing is observed in 16% of our whole array observations and 6.6% of our sub array observations.

3.1 Frequency dependence

Figure 6 shows the spatial variability of multipathing with different frequency bands. Some observations show clear multipathing within specific frequency bands while others in all frequency bands, which could be due to differences in the nature of the boundaries such as the velocity gradient, inclination or depth. As explained in Section 2.3, to observe multipathed arrivals, enough of the Fresnel zone needs to sample different velocities. This requires the lateral velocity gradient needs to be sufficiently strong, and sufficiently sampled by the wavefield.

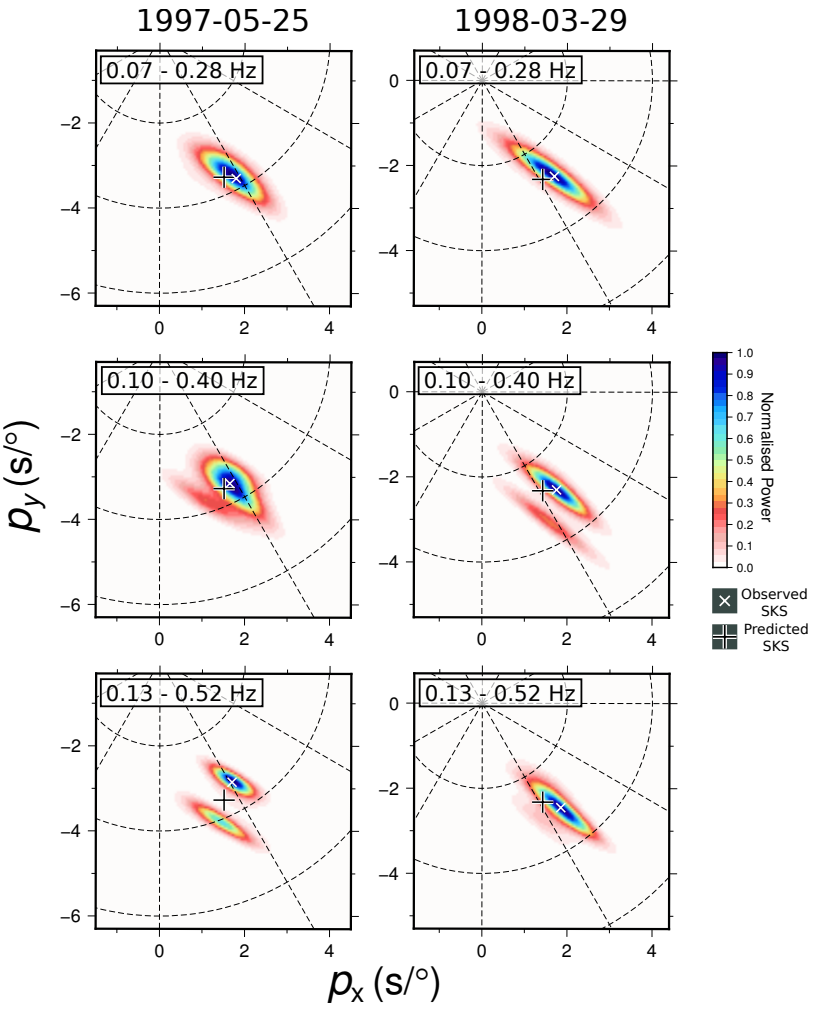

Figure 6. A comparison of the frequencies clear multipathing is observed for two different events. The left column shows θ-p plots using data from the 25 May 1997 event and clear multipathing is only observed in the 0.13 – 0.52 Hz band. The right column shows θ-p plots using data from the 29 March 1998 event where clear multipathing is only observed in the 0.10 – 0.40 Hz frequency band.

Observations of multipathing at high frequencies could be due to differences in wavelength or indicative of strong velocity gradients while multipathing at low frequencies indicative of a significant velocity change over a wider boundary. If the boundary is at an angle to the incidence of the wave, the boundary will not be sampled for as long and appear smoother.

Sampling boundaries at different depths could cause frequency variation in our observations due to changes of wavelength with velocity. At the same depth, and therefore the same 1-D velocity, the boundaries need to have different gradients or inclinations for multipathing to occur at different frequencies. At different depths, the boundaries could be the same sharpness and inclination, but observed at different frequencies due to different Fresnel zone sizes.

The size and station density of the array could contribute to the frequency variation. Larger, denser arrays will be sensitive to a larger area and will record multipathed arrivals in more waveforms. Lower frequencies with larger Fresnel volumes are more sensitive to weaker velocity gradients, but the weaker gradients may mean the multipathed arrivals will have a smaller amplitude also. Whole array observations should have more multipathing observations at lower frequencies (Figure 7) because weaker multipathed arrivals will be recorded in more waveforms and stack to an observable power.

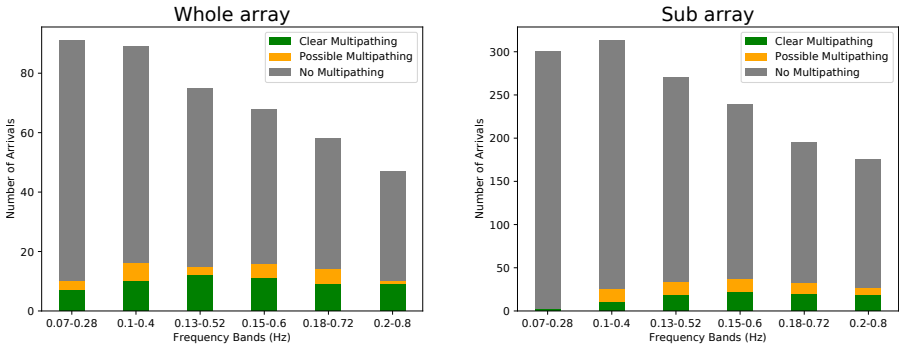

Figure 7. Number of observations of clear (green), possible (yellow) and no multipathing (grey) in different frequency bands for whole array and sub array observations. The number of usable observations changes with frequency due to noise conditions and slowness resolution. At higher frequencies the observations were noisier and at the lowest frequencies the slowness resolution is too poor to use.

3.2 Spatial analysis

Spatially analysing our observations shows multipathing is not limited to one region and occurs in different frequency bands depending on the region. In Figure 8, the loci and the tomography velocity contours for both whole and sub array observations align well to the east of Africa (25°S, 32°W) with a boundary trending northwest-southeast which then curves to trend approximately west-east as the boundary moves southward. In these regions, multipathing is observed in all frequency bands over both whole and sub array observations. The range of frequencies could be interpreted as an LLVP boundary being sampled at several depths, or a boundary with both a strong lateral velocity gradients and a significant velocity change.

The circular low velocity feature to the southeast of Africa (35°S, 30°W) marked by -1.5% δV_s velocity contour aligns well with the loci in the area. Multipathing is observed at a range of different frequencies here with arguably more observations at frequencies above the 0.15 – 0.60 Hz band. Observing multipathing at higher frequencies imply sampling of a relatively sharp gradient and observations in a broad frequency range suggest large and sharp velocity changes or sampling boundaries at several depths.

To the west of Africa (25°S, 15°W), particularly in the sub array observations, there is a lot of scatter in loci orientations and multipathing is mainly observed in the higher frequency bands. The scattered loci are possibly due to the waves travelling through the body of the LLVP boundaries and sampling boundaries at several depths. Depending on the depth, the boundaries could have different orientations, therefore leading to scattered loci. Observing multipathing in higher frequency bands could be due to strong lateral velocity gradients or the depths the boundaries have been sampled.

Studies using travel time and waveform observations have reported a boundary to the southwest of Africa with an approximate northwest-southeast strike (Ni et al., 2002). The orientation of the locus of our multipathed arrival in this region approximately agrees (Figure 8) supporting these previous results. Sun et al. (2010) find evidence for a mantle plume in the mid-mantle of this region too. We do not find evidence for this, most likely because of resolution and sampling limitations.

To further explore the spatial distribution of multipathing, we compare the locations of clear, possible and no multipathing observed at any frequency (Figure 9). Multipathing is not limited to one region and the pierce points of clear multipathing are very close to pierce points that show no or unclear multipathing. Our interpretation is the boundary structure needs to be sampled in a specific way for the multipathed arrivals to arrive with observable amplitudes.

3.3 Seismic anisotropy

There have been several studies analysing seismic anisotropy in the region of this study (e.g. Lynner & Long, 2014; Ford et al., 2015; Wang & Wen, 2007a; Reiss et al., 2019; Cottaar & Romanowicz, 2013). Shear wave splitting could complicate the waveforms and be misinterpreted as multipathing. Therefore, we measure SKS splitting in splitting time and direction of the fast axis, remove the measured effect and repeat the analysis for a selection of events. After the anisotropy correction, we still observe multipathing. For low SNR events, correcting for anisotropy reduced the quality of the observation. Since anisotropy alone is not the cause of observed multipathing and can reduce the quality of some observations, we do not correct for shear wave splitting.

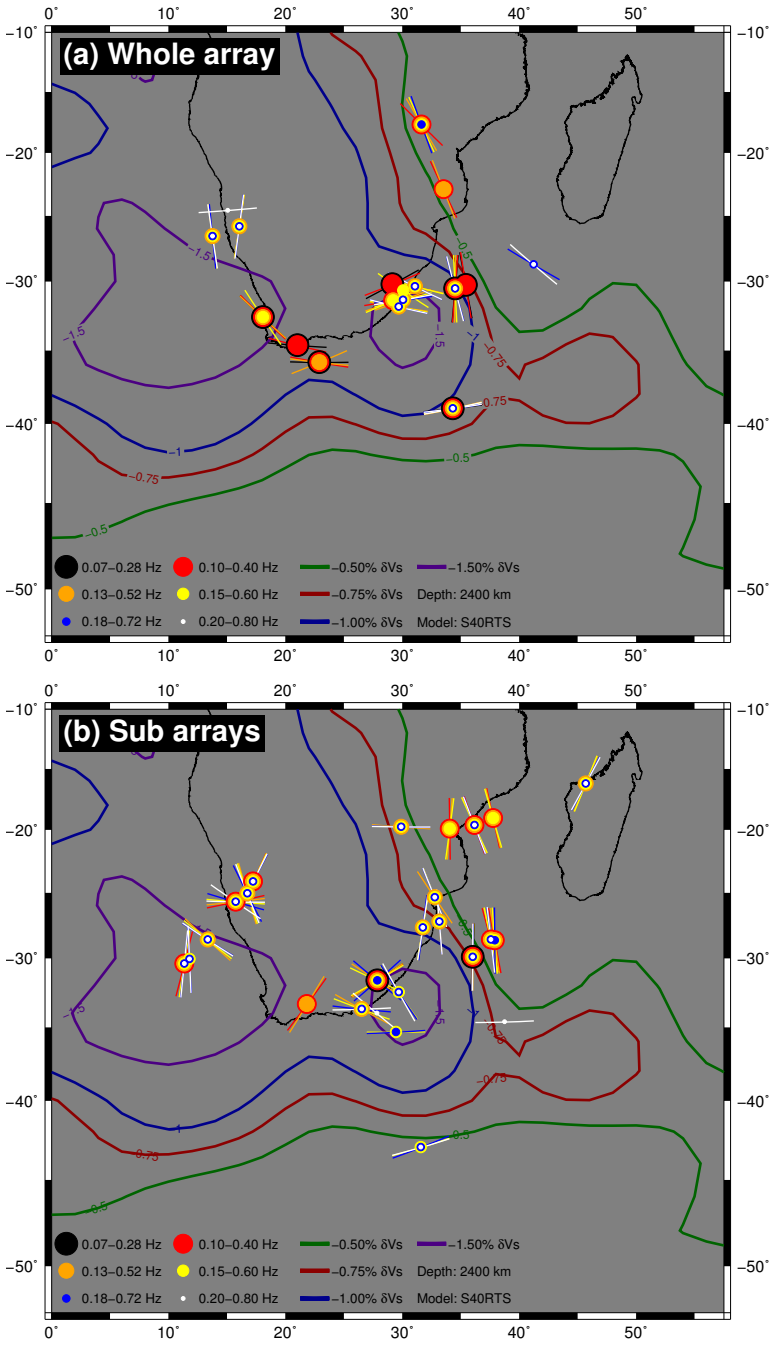

Figure 8. 1-D ray path pierce points at 2400 km depth (approximately 500 km above the CMB) for events showing clear multipathing. **(a)** whole array observations and **(b)** sub array observations. The size and colour of the circles correspond to the frequencies at which multipathing is observed. The locus between the arrivals is marked for each frequency to represent the approximate orientation of the boundary causing the multipathing. Velocity contours are shown at 2400 km depth from tomography model S40RTS (Ritsema et al., 2011).

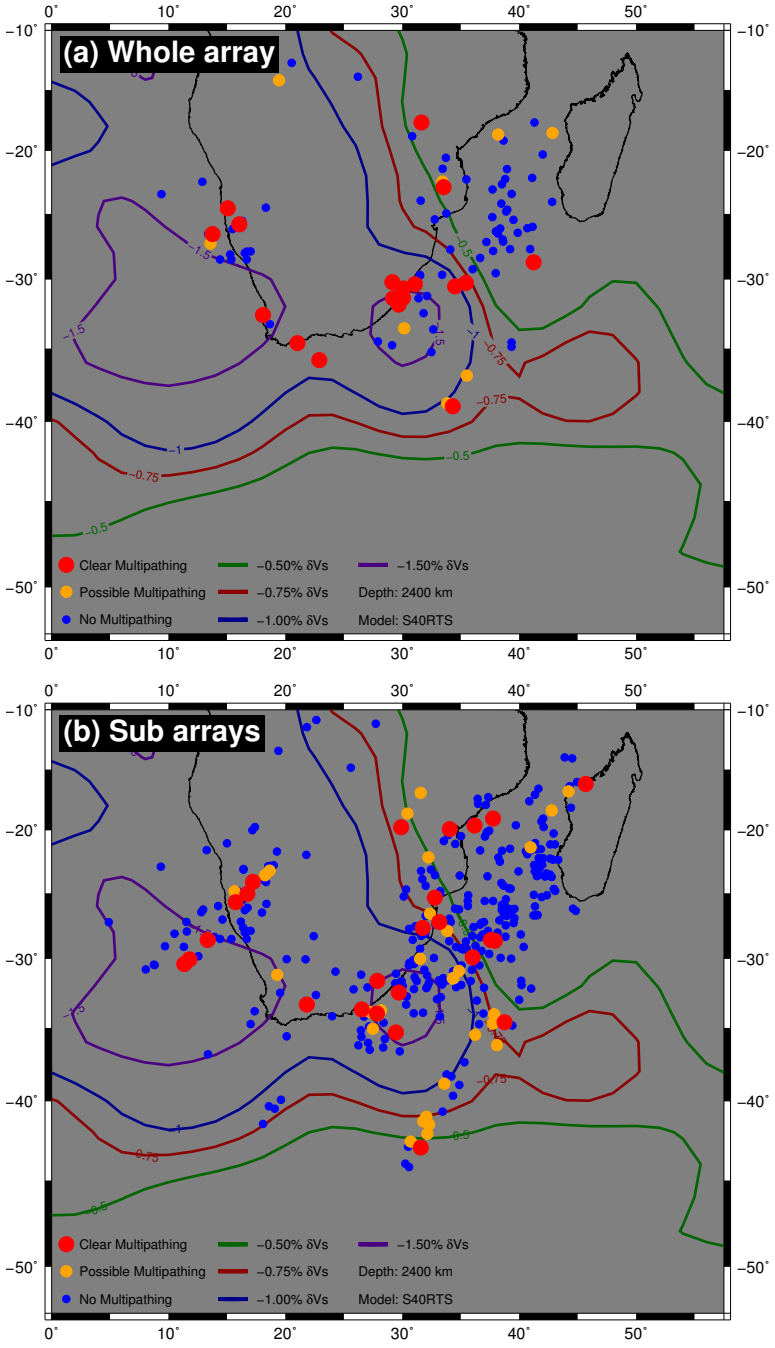

Figure 9. 1-D ray path pierce points at 2400 km depth (approximately 500 km above the CMB) with clear (red), possible (orange) and no (blue) multipathing at any frequency for **(a)**, whole array observations and **(b)** sub array observations. Clear multipathing at any frequency, it is labeled as 'clear', potential multipathing is labeled as 'possible', no indication of multipathing at any frequency is labeled as 'no' multipathing.

4 Slowness Vector Residuals

We spatially analyse backazimuth, horizontal slowness and slowness vector deviations to identify regions of wavefield perturbations. Descriptive interpretations are given in Sections 4.1 to 4.3. When analysing these deviations, the pierce point location is moved to match observed backazimuth and horizontal slowness.

4.1 Backazimuth Deviations

Spatial analysis of backazimuth deviations (Figure 10) reveals several patterns indicative of structures perturbing the wavefield. The most distinct pattern is to the southeast of Africa (35°S, 27°W) where positive backazimuth residuals (blue, arriving from more clockwise direction than predicted) to negative backazimuth residuals (red, arriving from more anticlockwise direction than predicted) then moving northeast (25°S, 40°W) to negligible backazimuth residuals (white, arriving as predicted). The transition from positive to negative residuals implies there are two boundaries being sampled causing diffraction in opposite directions. We interpret this as the circular structure southeast of Africa marked by the -1.5% δV_s velocity contours in Figure 10.

We detect more negative backazimuth residuals than positive (supplementary information) with the negative residuals also spread over a larger area. Some of the negative residuals could be caused by the same circular feature described above, but as the pierce point locations move northeast, the LLVP boundary trending in a northwest-southeast orientation could be contributing. Further north, the negative deviations sharply transition to negligible residuals implying they are not sampling a structure or boundary that would cause the wavefront to change direction. Either a boundary orthogonal to wave propagation or structures causing the wave to vertically refract with no change to the horizontal propagation direction are possibilities. We discuss this further when analysing the horizontal slowness deviations in Section 4.2.

Analysing the distribution of the backazimuth residuals shows little variation between frequency bands (supplementary information). The majority of the observations lying between approximately 8° and $-14°$ and maximum values of 10° to $-22°$ for positive and negative deviations respectively. There are more negative residual observations with on average approximately 64% negative residual observations compared to 36% positive. This is possibly because of the heterogeneous sampling from limited event-station configurations.

4.2 Horizontal slowness deviations

The spatial distribution of horizontal slowness residuals in Figure 11 offers a less clear picture than the backazimuth residuals. The circular feature defined by -1.5% δ V_s contours to the southeast of Africa (35°S, 30°W) does show some pattern with the negative residuals lying on the northwest side of the feature, closer to the array, and the positive residuals on the southeast side. Negative residuals mean the wave is arriving more steeply and positive residuals more shallowly, which is expected if the circular feature diffracts the waves.

Observations to the east of Africa (25°S, 40°W) show a transition from positive (green) to negative (red) residuals most of which also have very small backazimuth deviations. If the wave has passed through material that is slower or faster than the 1-D velocity value at that depth from PREM (Dziewonski & Anderson, 1981), the wave would refract to arrive at a different inclination and horizontal slowness, but with negligible backazimuth deviations. For the transition to be this abrupt, adjacent fast and slow structures such as slab remnants near a LLVP boundary would be needed. The location of fast structures relative to the LLVP boundary at the core-mantle boundary in tomography model SEMUCB-WM1 (French & Romanowicz, 2014) aligns well with the tran-

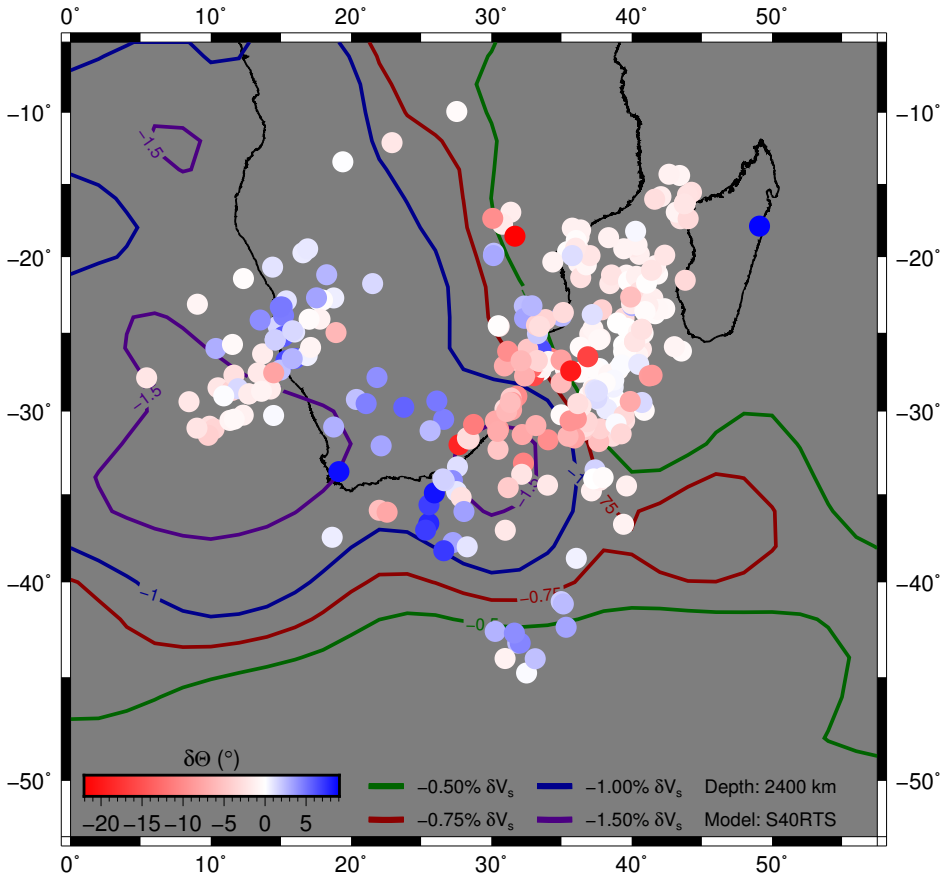

Figure 10. Pierce points for sub array observations (frequency band 0.13 Hz to 0.52 Hz) at 2400 km depth coloured by backazimuth deviations relative to the great circle path. Blue colours show paths that arrive from a more clockwise direction and red show paths arriving from a more anticlockwise direction than predicted. Contours from S40RTS (Ritsema et al., 2011) at a depth of 2400 km are shown to represent potential structures causing the observations. Pierce points are corrected to the measured horizontal slowness and backazimuth.

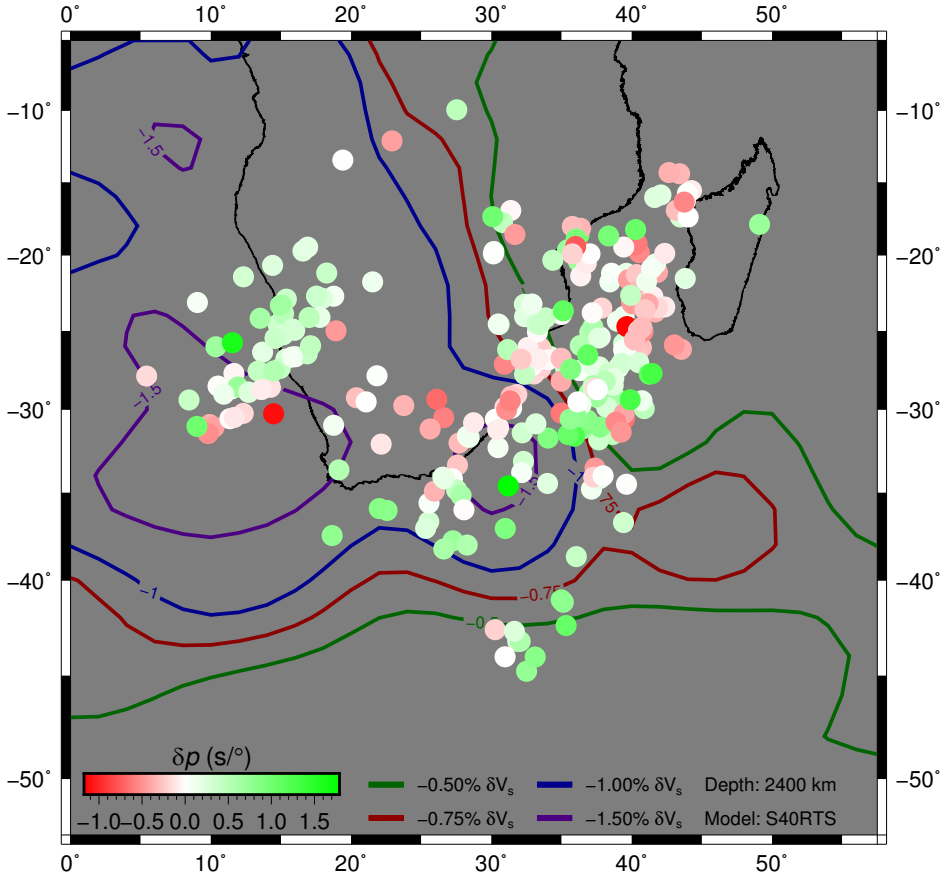

Figure 11. Pierce points for sub array observations (frequency band 0.13 Hz to 0.52 Hz) at 2400 km depth, coloured by horizontal slowness deviations relative to the PREM predicted ray parameter (Dziewonski & Anderson, 1981). Contours from S40RTS (Ritsema et al., 2011) at a depth of 2400 km are marked to outline structures potentially contributing to the observations. Pierce points are corrected to match the observed horizontal slowness and backazimuth.

sition (Figure 12), implying these structures could be the cause of our observations. Given the size of the sub-arrays and the size of the Fresnel zone at these frequencies, it is possible this fast structure is causing the waves to refract and arrive at a steeper inclination with negligible backazimuth deviation.

Residuals west of Africa (25°S, 15°W) are mainly positive, so arrive at a shallower angle, and travel through the body of the LLVP causing the waves to refract. However, there are also several multipathed arrivals in this region with scattered loci (Figure 8) suggesting the waves also sample a boundary but, because the loci are scattered, it is difficult to constrain exactly what is causing these observations.

The horizontal slowness deviations have little variation with frequency, with most observations lie between 1.2 s/° and −1.0 s/° (supplementary information). Outliers are present in these observations, but show no clear pattern and range from a maximum of 2.1 s/° and a minimum of −1.6 s/°. Like the backazimuth residuals, the observations are not evenly distributed about 0 s/° with 60% positive residuals and 40% negative. This variation could be due to the dominantly slow mantle structure beneath Africa causing them to refract and arrive at a shallower angle.

4.3 Full Slowness Vector Deviations

The full slowness vector deviation is a vector from the predicted arrival in the $\theta - p$ plot to the observed arrival. The azimuth of the vector indicates the direction of perturbation and the length is indicative magnitude. This vector combines the backazimuth and horizontal slowness perturbations giving a clear picture of how the wavefield is being affected. Figure 13 shows how these vectors vary spatially.

The radial pattern and magnitude of the vectors around the circular feature southeast of Africa (35°S, 30°W) support our interpretation that this structure is the cause of our observations. Northeast of this region, the azimuths change their orientation to be approximately orthogonal to the velocity contours of the boundary striking northwest-southeast. Further northeast (25°S, 40°W) the vectors have opposite azimuths shown by the colour change from red to green in the vector heads. The paths of these waves suggest they may not sample the LLVP boundary, supporting the hypothesis of fast and slow regions refracting the waves at depth. The vector residuals west of Africa (25°S, 15°W) are more scattered than in other regions but generally have an azimuth pointing away from the array and arrive at a shallower inclination. The scattered vector residuals, the scattered loci and the presence of multipathing in this region suggests the wavefield is being affected by several boundaries at different depths and the body of the LLVP.

The magnitude of the slowness vector deviations does not vary greatly with frequency with slightly more high magnitude deviations at higher frequencies and with minimum and maximum observed values from less than 0.1 s/° to 2.1 s/° (supplementary information).

Previous studies have analysed similar regions and show some evidence for structures we observe. Sun et al. (2009) analyse regions of the lowermost mantle similar to areas where we find boundaries between slow and fast structures and a quasi-circular structure. Using their multipath detector method with S_{diff} data from the 22 December 1997 event, they identify a region with strong gradients southeast of Africa in a similar region to the hypothesised boundary in Figure 12. Their travel time residuals transition from negative to positive over this region supports our interpretation of a transition from a slow to a fast structure. The results using data from the 04 September 1997 event show evidence for smaller scale structure southeast of the Kaapvaal array with a similar structure and approximate location as our observed circular structure.

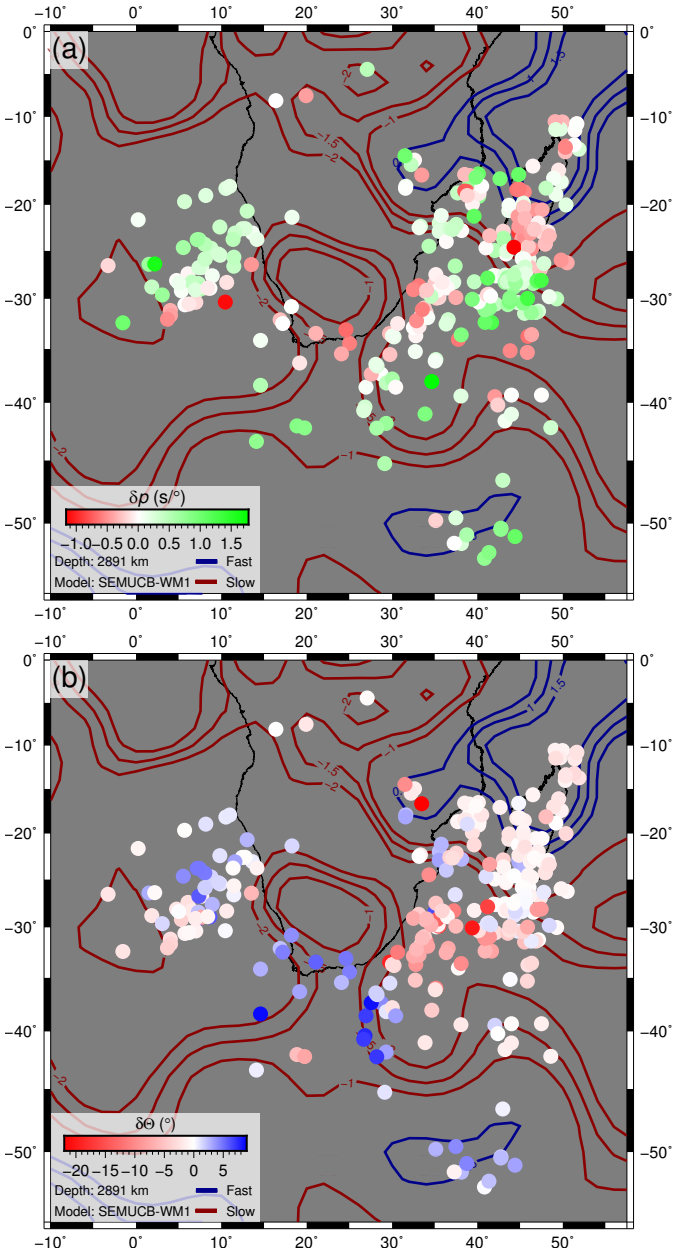

Figure 12. Pierce points at the CMB coloured with **(a)** horizontal slowness deviations and **(b)** backazimuth deviations. Negative contours −1.0%, −1.5%, −2.0% δV_s and positive contours 0.5%, 1.0%, 1.5% δV_s of tomography model SEMUCB-WM1 (French & Romanowicz, 2014) are shown to highlight the transition from fast to slow structures east of Africa. The events have been relocated so the 1-D paths arrive from the observed backazimuth and horizontal slowness.

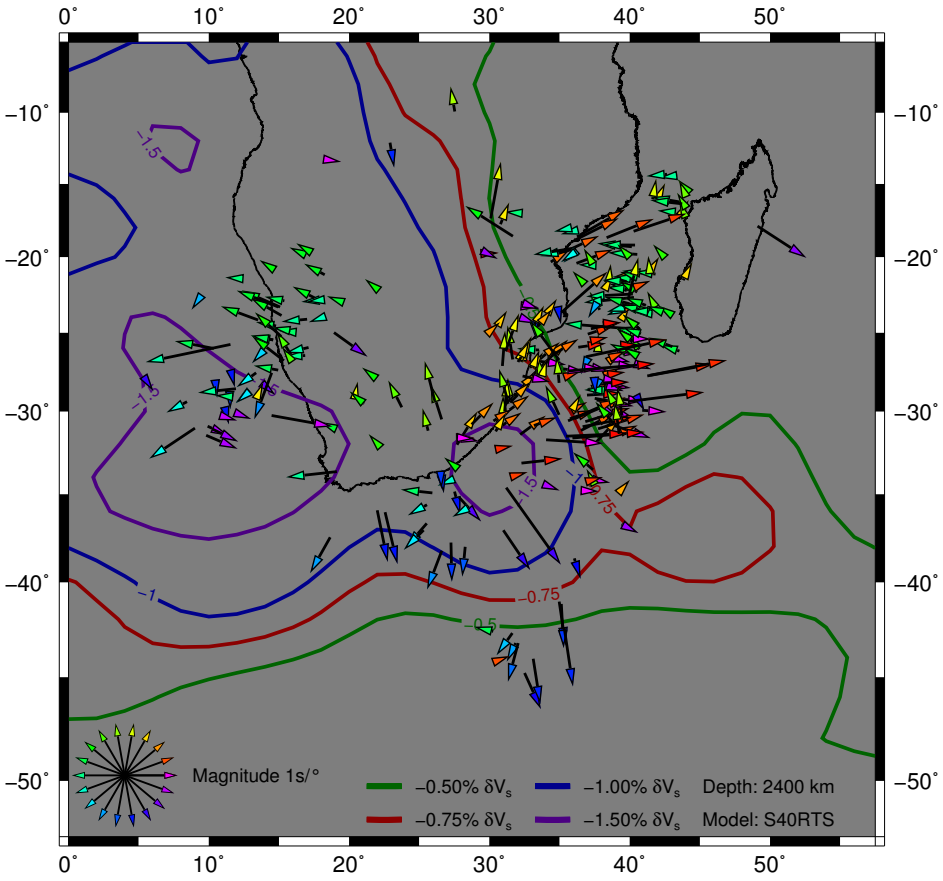

Figure 13. Pierce points for sub array observations showing the full slowness vector deviation from the prediction to the observation in the θ-p plot coloured by azimuth (Figure 4). The contours from S40RTS (Ritsema et al., 2011) and the pierce points are marked at a depth of 2400 km to outline potential structures contributing to the observations. The frequency band used is from 0.13 Hz to 0.52 Hz. The pierce points have been relocated according to the observed backazimuth and horizontal slowness.

5 Forward modelling and comparison to tomography models

This section explores the properties required to observe multipathing through forward modelling and compares our estimated velocity gradient to previous studies. The velocity gradients at the boundary of LLVPs are frequently used as evidence for chemical heterogeneity (e.g. Ni et al., 2002; To et al., 2005; Wen et al., 2001). These velocity gradients were estimated by replicating travel time residuals and waveforms via forward modelling. In this section, we replicate conditions for multipathing to be observed using this method and how these conditions compare to that of other studies (Table 1).

We use SPECFEM3D (Komatitsch & Tromp, 2002b, 2002a), to create synthetic data for three earthquakes (Section 5.1) which show multipathing at frequencies that can be modelled. As the modelling is computationally expensive, we limit ourselves to these events and model frequencies up to approximately 0.18 Hz. We test the effects of ellipticity and topography and find they have a negligible effect.

The loss of small-scale heterogeneity and reduction of velocity amplitude and gradients in seismic tomography from regularisation, smoothing and limited sampling coverage is well documented (Ritsema et al., 2007; Foulger et al., 2013; Schuberth et al., 2009; Bull et al., 2009). Given the large parameter space of a 3-D structure that could cause multipathing, we take the structure of tomography as an approximation of long-wavelength Earth structure and accept the mentioned limitations. From this starting point, we increase the velocity perturbations and gradients linearly to approximately account for the reduction through tomographic filtering and recreate conditions for multipathing to be observed in our method.

S40RTS (Ritsema et al., 2011) is used as a starting point as the velocity contours shown in figures in Sections 3 and 4 provide possible explanations for our observations. In each model, the velocity perturbations have been amplified at depths greater than 1000 km and depths shallower than 660 km are unchanged. The transition from the amplified lower mantle to the upper mantle is tapered to avoid artefacts. No crustal model is used in our modelling as test show no identifiable effect of crustal structure on our observations. Three models are used where perturbations at depths greater than 1000 km have been doubled (labeled as M2), trebled (M3), quadrupled (M4) and we use S40RTS (Ritsema et al., 2011) with no amplification (M1).

5.1 Gradients of boundaries

We compare observations of SKS data from events on the 25 May 1997, 28 March 1998 and 28 May 1997 to runs using all models described earlier. Figure 14 shows the $\theta - p$ plots of the synthetic data with the observations.

For all events, the S40RTS (Ritsema et al., 2011) velocity perturbations are not sufficient to cause detectable multipathing, indicating that stronger gradients are required. In models with stronger gradients, whether multipathing is observed and how similar it is to the observation varies with the event likely due to the different sampling geometry. Synthetic data for the 25 May 1997 in model M3 shows clear multipathing where the relative power and location of the two arrivals are similar to the observation. In model M2, there is no clear multipathing and the location of the arrival is approximately the average of the locations of the observed multipathed arrivals. As the only difference between M2 and M3 is the strength of amplitudes in the lower mantle, we argue it is lower mantle structure causing the observed multipathed arrivals in this event.

The 29 May 1997 event shows some weak multipathing in all amplified models in similar locations to the observation, but the arrivals do not have the same relative power in the $\theta - p$ plot. This suggests there is a boundary being sampled, but the gradient in the model is weaker or the pathlength along the boundary is shorter than in the data.

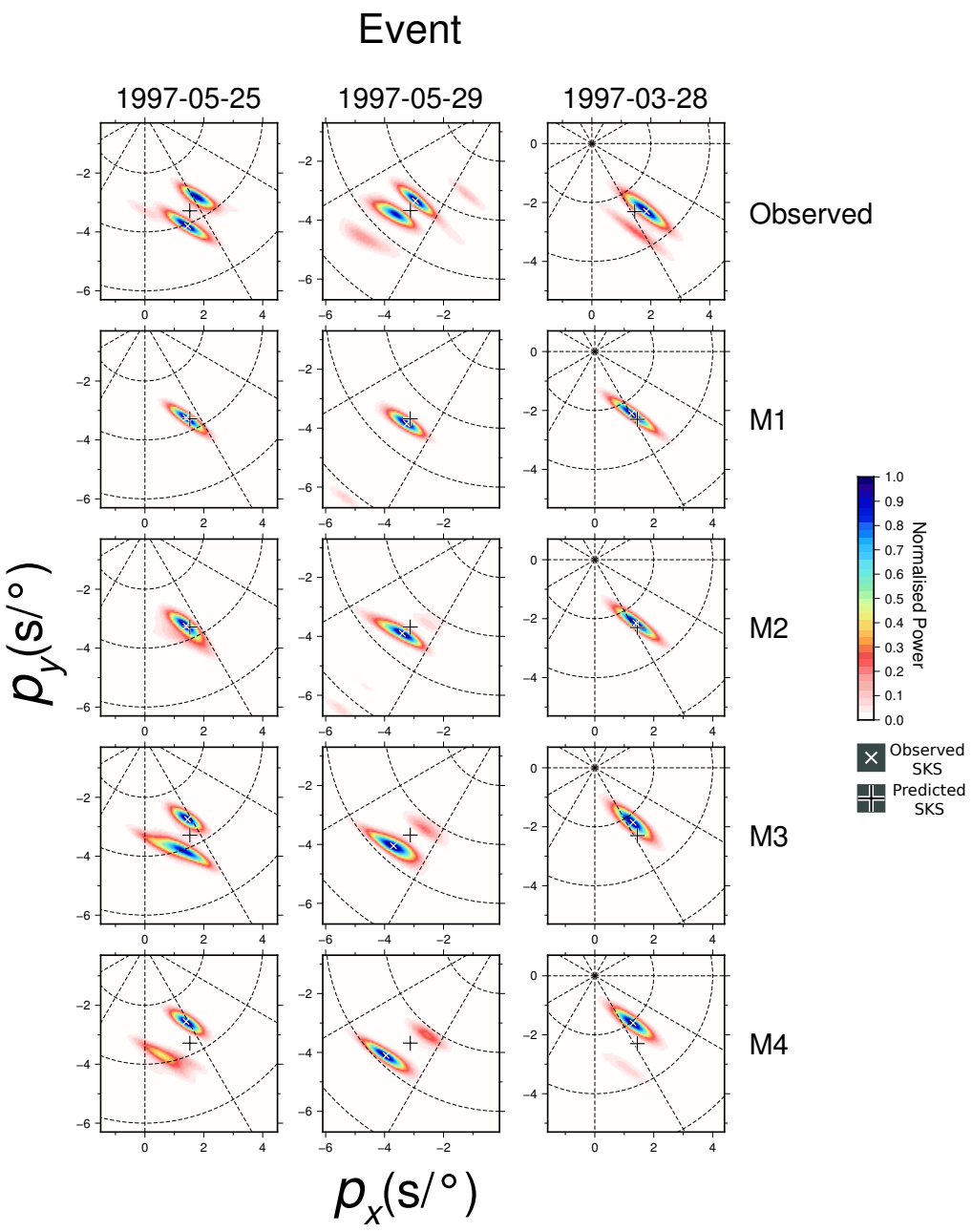

Figure 14. Analysis of multipathing for three events in the observed data (top row) with synthetics from models M1 to M4 in the rows beneath (labeled on the right). For each event, the same frequency bands are used for the observed and synthetic data.

The 29 March 1998 event shows no multipathing in most of the models except for M4, but this has much weaker multipathing and both arrivals are different to their location in the observation. The strength of the velocity gradient of the boundary or its location in the tomography is not enough to reproduce the observation.

These varying results are to be expected with the inherent limitations of tomography described earlier. Due to the good agreement between synthetic data from model M3 and real observation for the 25 May 1997 event, we analyse the gradients sampled by this model. The gradients sampled by the mean 1D raypath for the event at 25 km depth intervals in model M3 is shown in Figure 15. The largest gradients sampled are not at the CMB but approximately 600 km above it, a similar depth to the maximum misfit found by Zhao et al. (2015) in their analysis of waveform broadening and the Pacific LLVP. The maximum gradient sampled is 0.7% δV_s per 100 km (0.0005 km s^{-1} km^{-1}) about 600 km above the CMB. This is an order of magnitude lower than found in some previous studies, which we discuss further in Section 5.2.

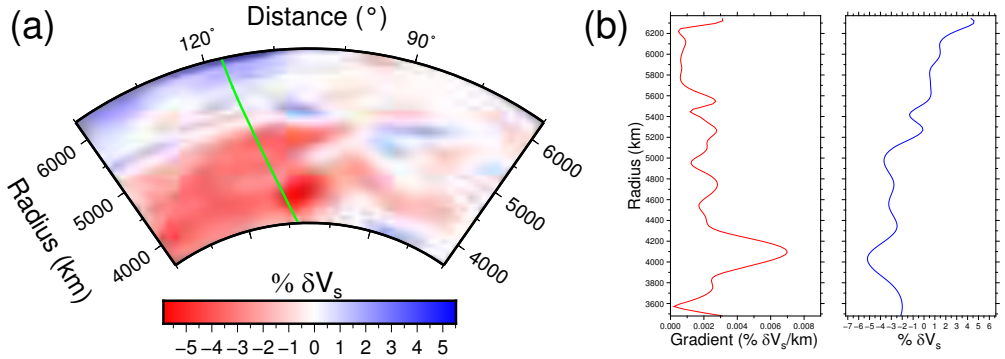

Figure 15. **(a)** Cross section of the receiver-side path of SKS from the 25 May 1997 event through M3. **(b)** two depth sections of the gradients and velocity perturbations sampled by the receiver-side 1-D path from event to average station location through model M3.

Although the modelled $\theta - p$ observation is similar, the modelled SKS data arrives much earlier than in the observations as shown in Figure 16. The difference in travel times is a reflection of the velocity perturbations sampled whereas the observation of multipathing is indicative of the gradients sampled. For this example, the gradient sampled over the raypath is sufficient to create similar multipathing as the observation, but the velocity perturbations are not sufficient to replicate the observed travel time residuals.

5.2 Comparison with previous studies

Many studies have analysed the African LLVP boundaries using travel time residuals and multipathing observations with forward modelling to infer properties such as the location, velocity gradient and inclination of the boundary (e.g. Ni et al., 2002; Sun & Miller, 2013; Sun et al., 2010; Ritsema et al., 1998; Wang & Wen, 2004). As there is extensive analysis of the structures in the regions we have analysed, we compare the findings of the relevant studies to our own.

From travel time residuals and waveform analysis, several studies have inferred the velocity gradients at the boundaries and perturbations inside the African LLVP (Ni et al., 2002; Sun & Miller, 2013; Wang & Wen, 2007b; Ritsema et al., 1998). We assume the gradient of the boundary is the main cause of the observed multipathing. As only one of our models matches well with the observation, we only compare the gradient we found to produce multipathing for the 25 May 1997 event with other studies (See Ta-

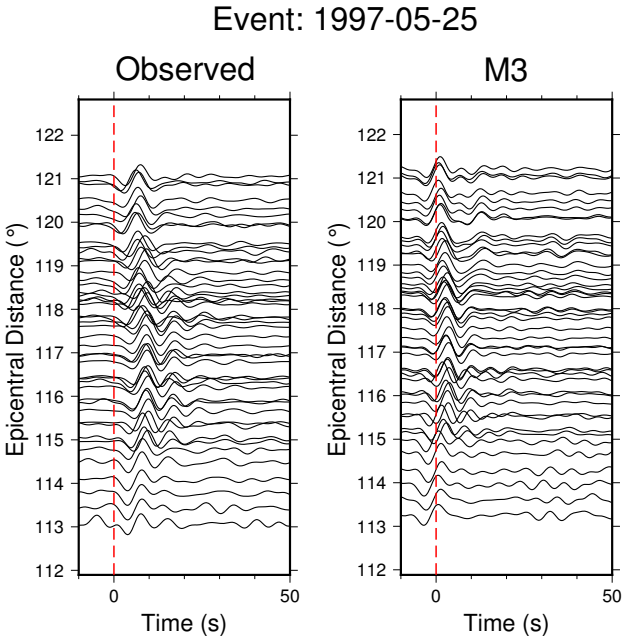

Figure 16. Record sections of the observed data (left) and the synthetic data from M3 (right) for the 25 May 1997 event. Despite producing multipathing in the $\theta - p$ plots, the travel time are much closer to the PREM (Dziewonski & Anderson, 1981) predicted SKS arrival time (dashed red line). The modeled waveforms arrive significantly earlier than the observations. We suggest the negative velocity perturbations in the model are not strong enough or the positive perturbations are too strong.

ble 1). Gradients up to 0.7% δV_s per 100 km (0.00050 km s^{-1} km^{-1}) are required to produce similar observations for the 25 May 1997 event which is an order of magnitude lower than the strongest estimated gradients of -3% δV_s per 50 km (0.044 km s^{-1} km^{-1}) (Ni et al., 2002), though similar to that found by Ritsema et al. (1998) -2% δV_s per 300 km (0.00048 km s^{-1} km^{-1}). We discuss possible reasons for this weaker gradient below.

Our observations analyse coherent signals across the array by stacking many waveforms together and not analysing them individually. Each measurement is sensitive to a larger region and could lead to boundary structures being sampled for longer, therefore weaker gradients are required to produce multipathing. Previous estimates of the stronger gradients used 2-D forward modelling to replicate their observations (Ni et al., 2002; Ni & Helmberger, 2003b). Any travel time delay or multipathing would have to be from in-plane structures and contributions from out of plane structure would not be accounted for. We use 3-D full wavefield modelling thus accounting for contributions from out of plane structures which could lead to a weaker gradient estimation. The effect of a wider region of influence from array methodology on a full wavefield sampling a 3-D anomaly structure could explain the difference between our gradient estimate and that of previous studies.

The presence of strong velocity gradients at LLVP boundaries causing multipathing and sharp changes in travel time residuals is commonly used as evidence for a thermochemical origin of LLVPs (Ni et al., 2002; To et al., 2005; Ritsema et al., 1998). We require gradients an order of magnitude lower than previous estimates to produce multipathing similar to our observations. The gradients of 0.7 % δV_s per 100 km (0.00050 km s^{-1} km^{-1}) are well below those evident in purely thermal models (2.25 % δV_s over 50

551 km (0.0032 km s^{-1} km^{-1}) (Schuberth et al., 2009) and 3.5 – 4.5 % δV_s per 100 km (0.0025
552 – 0.0032 km s^{-1} km^{-1}) (Davies et al., 2012)). This modelling implies that velocity gra-
553 dients capable of producing observable multipathing cannot distinguish between ther-
554 mal and thermochemical LLVPs.

6 Conclusions

Through measuring the backazimuth and horizontal slowness of SKS and SKKS data sampling the lower mantle beneath Africa, we identify clear multipathing in approximately 16 % of our whole array observations and 8.0 % of our sub array observations. We find evidence for wavefield perturbation from backazimuth deviations of up to 22° and horizontal slowness deviations of up to 1.2 $s/°$. Spatial analysis of these measurements relative to structure resolved by seismic tomography gives evidence for a circular feature to the southeast of Africa, adjacent fast and slow structures and an LLVP boundary. This suggests that tomography models, while limited, do resolve some structure that provide explanations for our observations.

We conduct full wavefield forward modelling to constrain what lateral velocity gradients are needed to reproduce our observations. We find gradients of up to 0.7 % δVs per 100 km (0.00050 km s^{-1} km^{-1}) sampled approximately 600 km above the CMB are required to reproduce our multipathing observations. This is an order of magnitude lower than previous estimates of -3% δV_s per 50 km (0.0044 km s^{-1} km^{-1}) (Ni et al., 2002), which is commonly used to argue for a thermochemical origin of LLVPs. As the gradients we predict are well below the largest estimates for both thermal and thermochemical structures (Davies et al., 2012), we argue multipathing observation caused by lateral velocity gradients of LLVP boundaries is not necessarily evidence for a thermochemical composition.

Acknowledgments

This research is supported by the NERC DTP Spheres grant NE/L002574/1. Predictions were made using the Taup toolkit (Crotwell et al., 1999). Figures made using GMT (Wessel et al., 2013). Data was retrieved from IRIS Data Center (http://www.iris.edu) using ObspyDMT (Hosseini & Sigloch, 2017), events used are provided in the supplementary material. There are no financial conflicts of interest for any authors.

References

Bijwaard, H., Spakman, W., & Engdahl, E. R. (1998). Closing the gap between regional and global travel time tomography. *Journal of Geophysical Research: Solid Earth*, *103*(B12), 30055–30078.

Blandford, R. R. (1974). An automatic event detector at the Tonto Forest seismic observatory. *Geophysics*, *39*(5), 633–643.

Bull, A. L., McNamara, A. K., Becker, T. W., & Ritsema, J. (2010). Global scale models of the mantle flow field predicted by synthetic tomography models. *Physics of the Earth and Planetary Interiors*, *182*(3-4), 129–138.

Bull, A. L., McNamara, A. K., & Ritsema, J. (2009). Synthetic tomography of plume clusters and thermochemical piles. *Earth and Planetary Science Letters*, *278*(3), 152–162.

Christensen, U. R., & Hofmann, A. W. (1994). Segregation of subducted oceanic crust in the convecting mantle. *Journal of Geophysical Research: Solid Earth*, *99*(B10), 19867–19884.

Cottaar, S., & Romanowicz, B. (2013). Observations of changing anisotropy across the southern margin of the African LLSVP. *Geophysical Journal International*, *195*(2), 1184–1195.

Crotwell, H. P., Owens, T. J., & Ritsema, J. (1999). The TauP Toolkit: Flexible seismic travel-time and ray-path utilities. *Seismological Research Letters*, *70*(2), 154–160.

Davaille, A. (1999). Simultaneous generation of hotspots and superswells by convection in a heterogeneous planetary mantle. *Nature*, *402*(6763), 756–760.

Davies, D. R., Goes, S., Davies, J. H., Schuberth, B. S. A., Bunge, H.-P., & Ritsema,

J. (2012). Reconciling dynamic and seismic models of Earth's lower mantle: The dominant role of thermal heterogeneity. *Earth and Planetary Science Letters*, *353*, 253–269.

Davies, D. R., Goes, S., & Lau, H. C. P. (2015). Thermally dominated deep mantle LLSVPs: a review. In *The earth's heterogeneous mantle* (pp. 441–477). Springer.

Davies, D. R., Goes, S., & Sambridge, M. (2015). On the relationship between volcanic hotspot locations, the reconstructed eruption sites of large igneous provinces and deep mantle seismic structure. *Earth and Planetary Science Letters*, *411*, 121–130.

Deschamps, F., Cobden, L., & Tackley, P. J. (2012). The primitive nature of large low shear-wave velocity provinces. *Earth and Planetary Science Letters*, *349*, 198–208.

Dziewonski, A. M., & Anderson, D. L. (1981). Preliminary reference Earth model. *Physics of the earth and planetary interiors*, *25*(4), 297–356.

Ford, H. A., Long, M. D., He, X., & Lynner, C. (2015). Lowermost mantle flow at the eastern edge of the African Large Low Shear Velocity Province. *Earth and Planetary Science Letters*, *420*, 12–22.

Foulger, G. R., Panza, G. F., Artemieva, I. M., Bastow, I. D., Cammarano, F., Evans, J. R., ... Yanovskaya, T. B. (2013). Caveats on tomographic images. *Terra Nova*, *25*(4), 259–281.

French, S. W., & Romanowicz, B. A. (2014). Whole-mantle radially anisotropic shear velocity structure from spectral-element waveform tomography. *Geophysical Journal International*, *199*(3), 1303–1327.

Frost, D. A., & Rost, S. (2014). The P-wave boundary of the large-low shear velocity province beneath the Pacific. *Earth and Planetary Science Letters*, *403*, 380–392.

Garnero, E. J., McNamara, A. K., & Shim, S.-H. (2016). Continent-sized anomalous zones with low seismic velocity at the base of Earth's mantle. *Nature Geoscience*, *9*(7), 481–489.

Grand, S. P. (2002). Mantle shear–wave tomography and the fate of subducted slabs. *Philosophical Transactions of the Royal Society of London A: Mathematical, Physical and Engineering Sciences*, *360*(1800), 2475–2491.

Grand, S. P., van der Hilst, R. D., & Widiyantoro, S. (1997). High resolution global tomography: a snapshot of convection in the Earth. *Geological Society of America Today*, *7*(4).

Hager, B. H. (1984). Subducted slabs and the geoid: Constraints on mantle rheology and flow. *Journal of Geophysical Research: Solid Earth*, *89*(B7), 6003–6015.

Hager, B. H., Clayton, R. W., Richards, M. A., Comer, R. P., & Dziewonski, A. M. (1985). Lower mantle heterogeneity, dynamic topography and the geoid. *Nature*, *313*(6003), 541.

He, Y., & Wen, L. (2009). Structural features and shear-velocity structure of the "Pacific Anomaly". *Journal of Geophysical Research: Solid Earth*, *114*(B2).

He, Y., & Wen, L. (2012). Geographic boundary of the "Pacific Anomaly" and its geometry and transitional structure in the north. *Journal of Geophysical Research: Solid Earth*, *117*(B9).

He, Y., Wen, L., & Zheng, T. (2006). Geographic boundary and shear wave velocity structure of the "Pacific anomaly" near the core–mantle boundary beneath western Pacific. *Earth and Planetary Science Letters*, *244*(1), 302–314.

Hirose, K., Fei, Y., Ma, Y., & Mao, H.-K. (1999). The fate of subducted basaltic crust in the Earth's lower mantle. *Nature*, *397*(6714), 53–56.

Hirose, K., Takafuji, N., Sata, N., & Ohishi, Y. (2005). Phase transition and density of subducted MORB crust in the lower mantle. *Earth and Planetary Science Letters*, *237*(1-2), 239–251.

Hosseini, K., & Sigloch, K. (2017). obspyDMT: a Python toolbox for retrieving and processing of large seismological datasets. *Solid Earth*, *8*.

Hutko, A. R., Bahavar, M., Trabant, C., Weekly, R. T., Fossen, M. V., & Ahern, T. (2017). Data products at the IRIS-DMC: Growth and usage. *Seismological Research Letters*, *88*(3), 892–903.

Ishii, M., & Tromp, J. (1999). Normal-Mode and Free-Air Gravity Constraints on Lateral Variations in Velocity and Density of Earth's Mantle. *Science*, *285*(5431), 1231–1236.

James, D., Fouch, M., VanDecar, J., Van Der Lee, S., & Group, K. S. (2001). Tectospheric structure beneath southern Africa. *Geophysical research letters*, *28*(13), 2485–2488.

Koelemeijer, P., Deuss, A., & Ritsema, J. (2017). Density structure of Earth's lowermost mantle from Stoneley mode splitting observations. *Nature Communications*, *8*.

Koelemeijer, P., Ritsema, J., Deuss, A., & Van Heijst, H.-J. (2015). SP12RTS: a degree-12 model of shear-and compressional-wave velocity for Earth's mantle. *Geophysical Journal International*, *204*(2), 1024–1039.

Komatitsch, D., & Tromp, J. (2002a). Spectral-element simulations of global seismic wave propagation–II. Three-dimensional models, oceans, rotation and self-gravitation. *Geophysical Journal International*, *150*(1), 303–318.

Komatitsch, D., & Tromp, J. (2002b). Spectral-element simulations of global seismic wave propagation–I. Validation. *Geophysical Journal International*, *149*(2), 390–412.

Krischer, L., Hutko, A. R., Van Driel, M., Stähler, S., Bahavar, M., Trabant, C., & Nissen-Meyer, T. (2017). On-demand custom broadband synthetic seismograms. *Seismological Research Letters*, *88*(4), 1127–1140.

Labrosse, S., Hernlund, J., & Coltice, N. (2007). A crystallizing dense magma ocean at the base of the Earth's mantle. *Nature*, *450*(7171), 866–869.

Lau, H. C., Mitrovica, J. X., Davis, J. L., Tromp, J., Yang, H.-Y., & Al-Attar, D. (2017). Tidal tomography constrains Earth's deep-mantle buoyancy. *Nature*, *551*(7680), 321.

Lee, C.-T. A., Luffi, P., Höink, T., Li, J., Dasgupta, R., & Hernlund, J. (2010). Upside-down differentiation and generation of a 'primordial' lower mantle. *Nature*, *463*(7283), 930–933.

Lekic, V., Cottaar, S., Dziewonski, A., & Romanowicz, B. (2012). Cluster analysis of global lower mantle tomography: A new class of structure and implications for chemical heterogeneity. *Earth and Planetary Science Letters*, *357*, 68–77.

Li, M., & McNamara, A. K. (2013). The difficulty for subducted oceanic crust to accumulate at the Earth's core-mantle boundary. *Journal of Geophysical Research: Solid Earth*, *118*(4), 1807–1816.

Lithgow-Bertelloni, C., & Silver, P. G. (1998). Dynamic topography, plate driving forces and the African superswell. *Nature*, *395*(6699), 269.

Lucy, L. B. (1974). An iterative technique for the rectification of observed distributions. *The Astronomical Journal*, *79*, 745.

Lynner, C., & Long, M. D. (2014). Lowermost mantle anisotropy and deformation along the boundary of the African LLSVP. *Geophysical Research Letters*, *41*(10), 3447–3454.

Masters, G., Laske, G., Bolton, H., & Dziewonski, A. (2000). The relative behavior of shear velocity, bulk sound speed, and compressional velocity in the mantle: implications for chemical and thermal structure. *Earth's deep interior: mineral physics and tomography from the atomic to the global scale*, 63–87.

Maupin, V. (2011). Upper-mantle structure in southern Norway from beamforming of Rayleigh wave data presenting multipathing. *Geophysical Journal International*, *185*(2), 985–1002.

McNamara, A. K., Garnero, E. J., & Rost, S. (2010). Tracking deep mantle reser-

voirs with ultra-low velocity zones. *Earth and Planetary Science Letters*, *299*(1), 1–9.

McNamara, A. K., & Zhong, S. (2004). Thermochemical structures within a spherical mantle: Superplumes or piles? *Journal of Geophysical Research: Solid Earth*, *109*(B7).

McNamara, A. K., & Zhong, S. (2005). Thermochemical structures beneath Africa and the Pacific Ocean. *Nature*, *437*(7062), 1136–1139.

Mound, J., Davies, C., Rost, S., & Aurnou, J. (2019). Regional stratification at the top of Earth's core due to core–mantle boundary heat flux variations. *Nature Geoscience*, *12*(7), 575–580.

Mulyukova, E., Steinberger, B., Dabrowski, M., & Sobolev, S. V. (2015). Survival of LLSVPs for billions of years in a vigorously convecting mantle: replenishment and destruction of chemical anomaly. *Journal of Geophysical Research: Solid Earth*, *120*(5), 3824–3847.

Ni, S., & Helmberger, D. V. (2003a). Further constraints on the African superplume structure. *Physics of the Earth and Planetary Interiors*, *140*(1-3), 243–251.

Ni, S., & Helmberger, D. V. (2003b). Ridge-like lower mantle structure beneath south Africa. *Journal of Geophysical Research: Solid Earth*, *108*(B2).

Ni, S., & Helmberger, D. V. (2003c). Seismological constraints on the South African superplume; could be the oldest distinct structure on Earth. *Earth and Planetary Science Letters*, *206*(1-2), 119–131.

Ni, S., Tan, E., Gurnis, M., & Helmberger, D. (2002). Sharp sides to the African superplume. *Science*, *296*(5574), 1850–1852.

Picozzi, M., Parolai, S., & Bindi, D. (2010). Deblurring of frequency–wavenumber images from small-scale seismic arrays. *Geophysical Journal International*, *181*(1), 357–368.

Reiss, M., Long, M., & Creasy, N. (2019). Lowermost Mantle Anisotropy Beneath Africa From Differential SKS-SKKS Shear-Wave Splitting. *Journal of Geophysical Research: Solid Earth*.

Richardson, W. H. (1972). Bayesian-based iterative method of image restoration. *JOSA*, *62*(1), 55–59.

Ritsema, J., Deuss, A. A., Van Heijst, H. J., & Woodhouse, J. H. (2011). S40RTS: a degree-40 shear-velocity model for the mantle from new Rayleigh wave dispersion, teleseismic traveltime and normal-mode splitting function measurements. *Geophysical Journal International*, *184*(3), 1223–1236.

Ritsema, J., McNamara, A. K., & Bull, A. L. (2007). Tomographic filtering of geodynamic models: Implications for model interpretation and large-scale mantle structure. *Journal of Geophysical Research: Solid Earth*, *112*(B1).

Ritsema, J., Ni, S., Helmberger, D. V., & Crotwell, H. P. (1998). Evidence for strong shear velocity reductions and velocity gradients in the lower mantle beneath Africa. *Geophysical Research Letters*, *25*(23), 4245–4248.

Rost, S., & Thomas, C. (2002). Array seismology: Methods and applications. *Reviews of geophysics*, *40*(3).

Roy, S. K., Takeuchi, N., Srinagesh, D., Ravi Kumar, M., & Kawakatsu, H. (2019). Topography of the western Pacific LLSVP constrained by S-wave multipathing. *Geophysical Journal International*, *218*(1), 190–199.

Schimmel, M., & Paulssen, H. (1997). Noise reduction and detection of weak, coherent signals through phase-weighted stacks. *Geophysical Journal International*, *130*(2), 497–505.

Schubert, G., Masters, G., Olson, P., & Tackley, P. (2004). Superplumes or plume clusters? *Physics of the Earth and Planetary Interiors*, *146*(1), 147–162.

Schuberth, B. S. A., Bunge, H.-P., & Ritsema, J. (2009). Tomographic filtering of high-resolution mantle circulation models: Can seismic heterogeneity be explained by temperature alone? *Geochemistry, Geophysics, Geosystems*, *10*(5).

Silver, P. G., & Chan, W. W. (1986). Observations of body wave multipathing from broadband seismograms: evidence for lower mantle slab penetration beneath the Sea of Okhotsk. *Journal of Geophysical Research: Solid Earth*, *91*(B14), 13787–13802.

Simmons, N. A., Forte, A. M., Boschi, L., & Grand, S. P. (2010). GyPSuM: A joint tomographic model of mantle density and seismic wave speeds. *Journal of Geophysical Research: Solid Earth*, *115*(B12).

Su, W.-j., & Dziewonski, A. M. (1997). Simultaneous inversion for 3-D variations in shear and bulk velocity in the mantle. *Physics of the Earth and Planetary Interiors*, *100*(1-4), 135–156.

Sun, D., Gurnis, M., Saleeby, J., & Helmberger, D. (2017). A dipping, thick segment of the Farallon Slab beneath central US. *Journal of Geophysical Research: Solid Earth*, *122*(4), 2911–2928.

Sun, D., Helmberger, D., & Gurnis, M. (2010). A narrow, mid-mantle plume below southern Africa. *Geophysical Research Letters*, *37*(9).

Sun, D., Helmberger, D., Lai, V. H., Gurnis, M., Jackson, J. M., & Yang, H.-Y. (2019). Slab Control on the Northeastern Edge of the Mid-Pacific LLSVP near Hawaii. *Geophysical Research Letters*.

Sun, D., Helmberger, D., Ni, S., & Bower, D. (2009). Direct measures of lateral velocity variation in the deep Earth. *Journal of Geophysical Research: Solid Earth*, *114*(B5).

Sun, D., & Miller, M. S. (2013). Study of the western edge of the African large low shear velocity province. *Geochemistry, Geophysics, Geosystems*, *14*(8), 3109–3125.

Tackley, P. J. (1998). Three-Dimensional Simulations of Mantle Convection with a Thermo-Chemical Basal Boundary Layer: D″? *The core-mantle boundary region*, 231–253.

Tackley, P. J. (2011). Living dead slabs in 3-D: The dynamics of compositionally-stratified slabs entering a "slab graveyard" above the core-mantle boundary. *Physics of the Earth and Planetary Interiors*, *188*(3-4), 150–162.

Thorne, M. S., Garnero, E. J., & Grand, S. P. (2004). Geographic correlation between hot spots and deep mantle lateral shear-wave velocity gradients. *Physics of the Earth and Planetary Interiors*, *146*(1), 47–63.

To, A., Romanowicz, B., Capdeville, Y., & Takeuchi, N. (2005). 3D effects of sharp boundaries at the borders of the African and Pacific Superplumes: Observation and modeling. *Earth and Planetary Science Letters*, *233*(1), 137–153.

Tolstikhin, I., & Hofmann, A. W. (2005). Early crust on top of the earth's core. *Physics of the Earth and Planetary Interiors*, *148*(2-4), 109–130.

Torsvik, T. H., Burke, K., Steinberger, B., Webb, S. J., & Ashwal, L. D. (2010). Diamonds sampled by plumes from the core-mantle boundary. *Nature*, *466*(7304), 352–355.

Wang, Y., & Wen, L. (2004). Mapping the geometry and geographic distribution of a very low velocity province at the base of the Earth's mantle. *Journal of Geophysical Research: Solid Earth*, *109*(B10).

Wang, Y., & Wen, L. (2007a). Complex seismic anisotropy at the border of a very low velocity province at the base of the Earth's mantle. *Journal of Geophysical Research: Solid Earth*, *112*(B9).

Wang, Y., & Wen, L. (2007b). Geometry and P and S velocity structure of the "African Anomaly". *Journal of Geophysical Research: Solid Earth*, *112*(B5).

Wen, L., Silver, P., James, D., & Kuehnel, R. (2001). Seismic evidence for a thermo-chemical boundary at the base of the Earth's mantle. *Earth and Planetary Science Letters*, *189*(3), 141–153.

Wessel, P., Smith, W. H., Scharroo, R., Luis, J., & Wobbe, F. (2013). Generic mapping tools: improved version released. *Eos, Transactions American Geophysical Union*, *94*(45), 409–410.

824 Zhao, C., Garnero, E. J., McNamara, A. K., Schmerr, N., & Carlson, R. W. (2015).
825 Seismic evidence for a chemically distinct thermochemical reservoir in Earth's
826 deep mantle beneath Hawaii. *Earth and Planetary Science Letters*, *426*, 143–
827 153.